Flow structures and vertical transport in tilting salt fingers with a background shear

Junyi Li⊙ and Yantao Yang⊙[*]

State Key Laboratory for Turbulence and Complex Systems and Department of Mechanics and Engineering Science, College of Engineering, Peking University, Beijing 100871, People's Republic of China
and Joint Laboratory of Marine Hydrodynamics and Ocean Engineering, Pilot National Laboratory for Marine Science and Technology (Qingdao), Shandong 266237, People's Republic of China

In this work we study the fingering double diffusive convection, namely, the buoyancy-driven convection flow within a fluid layer experiencing an unstable salinity gradient and a stable thermal gradient. In particular, we investigate the influences from a background shear with uniform strength. Linear stability analysis indicates that the unstable modes shift from a circular shape to a sheetlike shape as the shear becomes stronger. Three-dimensional direct numerical simulations are conducted for five groups of cases, each of which has the same combination of thermal and salinity gradients (measured by corresponding Rayleigh numbers) and gradually increasing shear strength. The same properties of seawater are used for all simulations, i.e., the Prandtl number $\mathrm{Pr} = 7$ (the ratio of kinematic viscosity to thermal diffusivity) and the Schmidt number $\mathrm{Sc} = 700$ (the ratio of kinematic viscosity to salinity diffusivity). Numerical results reveal that a very weak shear organizes the salt fingers into a very regular pattern, which enhances the salinity flux. This enhancement effect, however, reduces as the Rayleigh number increases. For stronger shear the dominant structures shift from salt fingers to salt sheets, and the coherence length scale increases in the streamwise direction. Meanwhile, salinity and heat fluxes decrease. These findings suggest that even a weak shear can notably alter the morphology and transport properties of fingering double diffusive convection.

I. INTRODUCTION

When fluid density depends on two scalar components, buoyancy-driven convection happens in the form of double diffusive convection (DDC). DDC is ubiquitous in the ocean since the density of seawater is determined mainly by temperature and salinity [1–3]. In the upper water of many tropical and subtropical oceans, salinity and temperature decrease as the depth increases [4]. In these regions DDC happens in the finger regime, since the slow-diffusing salinity gradient drives the flow and the fast-diffusing temperature gradient stabilizes the flow [5]. DDC is very important for the vertical mixing and transport in the ocean and many other environments, as comprehensively discussed in the book by Radko [6] and the very recent review paper [7].

In real ocean environments, horizontal currents are omnipresent and inevitably interact with DDC motions, especially for the finger regime. For instance, observations have found nearly horizontal small-scale laminas in the salt-finger unstable region of the western North Atlantic [8,9]. The authors assume these structures to be the salt fingers tilted by background shear. Investigations also confirm

---

[*]yantao.yang@pku.edu.cn

that the moderate shear indeed appears in the high-gradient interfaces of such regions, with typical Richardson number of Ri $\geqslant 1$ [10]. Other evidences of the existence of tilted fingers include the vertical and sloping filaments found in the eastern North Atlantic [11]. All these observations indicate that the morphology and transport properties of fingers will be affected by the shear in the ocean.

Over the years people have confirmed the abundant interactions between the salt fingers and the background shear. The first systematic study, including experiments and theoretical analyses, of the shear effects on salt fingers was conducted by Linden [12]. The author states that the steady uniform shear will dampen the DDC disturbances along the streamwise direction, leading to the two-dimensional structure, namely, the salt sheet. Through linear stability analysis, such two-dimensional rolls are proved to be the most unstable mode in a finger regime under the shear with no inflection points [13]. For the inflectional shear, the flow is susceptible to the Kelvin-Helmholtz (KH) instability, which can coexist with the salt sheets [14]. The fully nonlinear numerical simulations show that the KH instability has a more lenient criterion with Ri exceeding unity under the DDC motions [15]. Other three-dimensional direct numerical simulations (DNSs) also demonstrate that two secondary instabilities will appear after the formation of salt sheets, which are called zigzag and tip modes [16,17]. The former may explain the origin of the oceanic horizontal bands mentioned above [8,18]. As the morphology of salt fingers undergoes various variations under the action of background shear, their transport efficiency also changes accordingly.

The key question about the sheared salt fingers is how the scalar transport capacity varies with the shear strength. It is natural to assume that the heat and salinity fluxes will decrease to a two-dimensional level when the salt sheets form, and Radko *et al.* [19] reach this conclusion by DNS with the stochastic shear related to the internal wave in the real ocean. However, this is not always the case when the salt sheets do not totally appear, or the secondary instabilities occur. In addition, the experimental and numerical settings will also affect the transport properties a lot. For instance, the experiments of Linden [12] reveal that the fluxes are even enhanced under the shear, which may be due to the working fluid flowing in and out of the domain constantly. Fernandes and Krishnamurti [20] conducted experiments and observed that the salinity flux decreases with the shear strength, and the heat flux eventually decreases to a total molecular diffusive mode. Through DNS in a sharp high-gradient interface, Kimura and Smyth analyze the transport properties for the salt sheets in which secondary instabilities appear, and they conclude that the effective diffusivities of heat and salt decrease with the shear strength and the density ratio [16,21]. Recently Sichani *et al.* [22] conducted a series of DNSs for the bounded sheared fingers within two horizontal plates, and they still found reduced salinity fluxes. Some models are proposed to explain the declined fluxes [9,23], but a general theory is still lacking for the various morphology of the sheared fingers. Moreover, the Richardson number in these studies is constrained in relatively small values. The situation with weak shear (or large Richardson number) is rarely explored.

It may be natural to assume that weak shear should not have notable influence. However, in this study we will show that even a relatively weak shear can significantly alter the flow morphology, making the salt fingers arranged regularly. With the increase of shear strength, the salinity flux first increases due to the orderly structure, and then decreases when the salt sheets form. The similar nonmonotonic variation is also reported in the recent sheared Rayleigh-Bénard convection (SRBC) studies [24,25]. In such systems the weak shear dampens the heat transport by destroying the thermal convection rolls, while the strong shear totally changes the flow morphology and enhances the transport. Jin *et al.* [26] further investigated SRBC with the rough boundaries, in which the weak shear first serves as a conveyor belt that strengths the thermal circulation and heat transport before disturbing it. Based on our previous work for fingering DDC [27], here we investigate the fingering DDC under the influence of background shear flow with a series of large Richardson numbers of Ri ~ 1–10^6. The Prandtl number and the Schmidt number, defined as the respective ratio of kinematic viscosity to the diffusivities of temperature and salinity, are set as the typical values for seawater at Pr $= 7$ and Sc $= 700$. Different density ratios and Rayleigh numbers are then simulated.
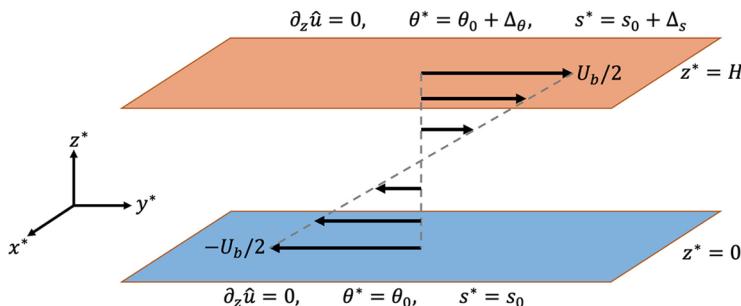
FIG. 1. Sketch of the domain geometry and flow setup. In the horizontal directions the periodic boundary condition is used for all flow quantities.

The lower bound of Ri is for the stage when the salt sheets just begin to appear, and is far from the criteria for KH instability. Thus in the current study we do not consider the secondary instabilities or the KH instability. We focus on the changes of the finger structures and the transport fluxes in the vertical direction under the relatively weak shear.

This paper is organized as follows. In Sec. II we introduce the governing equations and the related control domain. Next we conduct the linear stability analysis in Sec. III. Then Sec. IV presents the results of fully nonlinear simulations. Finally we give the conclusions in Sec. V.

II. GOVERNING EQUATIONS

We consider the incompressible Navier-Stokes equations for a fluid layer bounded by two horizontal plates which are separated by a height of H. A brief sketch of the flow domain is shown in Fig. 1. Let z^* be the normal direction of the plates ($z^* = 0$ at the bottom and $z^* = H$ at the top), while x^* and y^* are the horizontal directions. Hereafter, the asterisk ($*$) stands for the quantities in dimensional form, and the (x^*, y^*, z^*) directions are referred as spanwise, streamwise, and vertical directions, respectively. Gravity is oriented along the negative vertical direction. A uniform and steady background shear is sustained in the streamwise direction as $\mathbf{U}_s = S(z^* - H/2)\mathbf{e}_y$. Here S is the shear strength and $\mathbf{e}_y$ is the streamwise unit vector, respectively. The total velocity then reads $\mathbf{u}^* = \hat{\mathbf{u}} + \mathbf{U}_S = \hat{\mathbf{u}} + S(z^* - H/2)\mathbf{e}_y$. The shear strength can be written as $S = U_b/H$, which is achieved by imposing streamwise velocity $\pm U_b/2$ at the top and bottom plates, respectively. We use the linear equation of state as $\rho = \rho_0(1 - \beta_\theta \theta^* + \beta_s s^*)$, where ρ_0 is the reference value for the density. The temperature θ^* and the salinity s^* are also relative to the values of the reference state. β_θ is the thermal expansion coefficient and β_s is the coefficient of the density increase due to salinity change. The governing equations for the incompressible velocity $\hat{\mathbf{u}}$ and the two scalar components then read, under the Oberbeck-Boussinesq assumption,

$$\partial_t \hat{u}_i + \hat{u}_j \partial_j \hat{u}_i + U_{Sj} \partial_j \hat{u}_i + \hat{u}_j \partial_j U_{Si} = -\partial_i p^* + \nu \partial_j^2 \hat{u}_i + g\delta_{iz^*}(\beta_\theta \theta^* - \beta_s s^*), \tag{1a}$$

$$\partial_t \theta^* + \hat{u}_j \partial_j \theta^* + U_{Sj} \partial_j \theta^* = \kappa_\theta \partial_j^2 \theta^*, \tag{1b}$$

$$\partial_t s^* + \hat{u}_j \partial_j s^* + U_{Sj} \partial_j s^* = \kappa_s \partial_j^2 s^*, \tag{1c}$$

$$\partial_j \hat{u}_j = 0, \tag{1d}$$

in which $\hat{u}_i$ with $i = x^*, y^*, z^*$ are the three components of the perturbation velocity, p^* is kinematic pressure, ν is kinematic viscosity, g is the gravitational acceleration, and κ_θ and κ_s are the diffusivities of the temperature and the salinity, respectively. The density has been absorbed in the pressure term of Eq. (1a).

The temperature and the salinity are kept constant on the top and bottom plates, with the scalar differences across the fluid layer as Δ_θ and Δ_s, respectively. For the flow in the fingering regime, the

top plate has higher temperature and salinity. Therefore, the convection flow is driven by the salinity field but stabilized by the temperature field. For the velocity $\hat{\mathbf{u}}$ on the two plates the stress-free condition is applied for the streamwise and spanwise components, with no penetration condition for the normal component, respectively. Periodic conditions are used in the two horizontal directions. All the variables are nondimensionalized by the free-fall velocity $\sqrt{g\beta_s\Delta_s H}$, the domain height H, and the scalar differences Δ_θ and Δ_s. Then the nondimensional equations are

$$\partial_t u_i + u_j\partial_j u_i + \frac{(z-1/2)}{\sqrt{\mathrm{Ri}}}\partial_y u_i + \frac{1}{\sqrt{\mathrm{Ri}}}\delta_{iy}u_z = -\partial_i p + \frac{\sqrt{\mathrm{Sc}}}{\sqrt{\mathrm{Ra}}}\partial_j^2 u_i + \delta_{iz}(\Lambda\theta - s), \tag{2a}$$

$$\partial_t\theta + u_j\partial_j\theta + \frac{(z-1/2)}{\sqrt{\mathrm{Ri}}}\partial_y\theta = \frac{\sqrt{\mathrm{Sc}}}{\sqrt{\mathrm{RaPr}}}\partial_j^2\theta, \tag{2b}$$

$$\partial_t s + u_j\partial_j s + \frac{(z-1/2)}{\sqrt{\mathrm{Ri}}}\partial_y s = \frac{1}{\sqrt{\mathrm{RaSc}}}\partial_j^2 s, \tag{2c}$$

$$\partial_j u_j = 0, \tag{2d}$$

in which several control parameters are present. Throughout the current study we set the Prandtl number $\mathrm{Pr} = \nu/\kappa_\theta = 7$ and the Schmidt number $\mathrm{Sc} = \nu/\kappa_s = 700$, which are the typical values of seawater. The strength of the driving salinity gradient is measured by saline Rayleigh number, $\mathrm{Ra} = \beta_s g\Delta_s H^3/(\kappa_s\nu)$. The relative strength of the stabilizing temperature gradient is measured by the density ratio $\Lambda = \beta_\theta\Delta_\theta/\beta_s\Delta_s$. In addition, the background shear is characterized by the Richardson number $\mathrm{Ri} = \beta_s g\Delta_s H/U_b^2$. Note that stronger shear corresponds to smaller Ri.

It should be pointed out that, in the current wall-bounded model, the total density ratio defined by the temperature and salinity differences between the two horizontal plates is different from that defined by the background temperature and salinity gradients in the unbounded model [5,6]. In the current configuration, boundary layers develop adjacent to the two plates and sustain certain temperature and salinity differences. Therefore, the actual scalar differences and the resulting density ratio across the salt-finger layer in bulk are not equal to those prescribed between the two plates, but are the results of the interactions between the boundary layers and fingering bulk. It is then not surprising that in such a wall-bounded model fingers still grow even if the total density ratio between the two plates is smaller than unity, as observed in several experiments and our previous simulations [27–30].

In the following sections we will first make a linear stability analysis for governing equations (2) to identify the unstable parameter region and relevant unstable modes. Then we use our in-house DNS code to numerically solve the full nonlinear equations in the relevant parameter space. Some comparison will be made between the stability analyses and fully nonlinear simulations.

III. LINEAR STABILITY ANALYSIS

We now conduct a linear stability analysis for the nondimensionalized governing equations (2). The standard normal mode method is utilized. That is, the flow variables are decomposed as $\psi = \bar{\psi} + \psi'$, where $\bar{\psi}$ is the base state and ψ' is the perturbation, respectively. For the current flow, the base state is chosen to be the background shear flow with a vertically linear distribution for both temperature and salinity, i.e.,

$$\bar{\mathbf{u}} = \frac{z-1/2}{\sqrt{\mathrm{Ri}}}\mathbf{e}_y, \quad \bar{\theta} = z, \quad \bar{s} = z, \tag{3}$$

in which $z \in [0, 1]$. In Eqs. (2) one can treat the velocity deviating from the uniform shear flow as the perturbation velocity. Then substituting the base state into the governing equations and neglecting
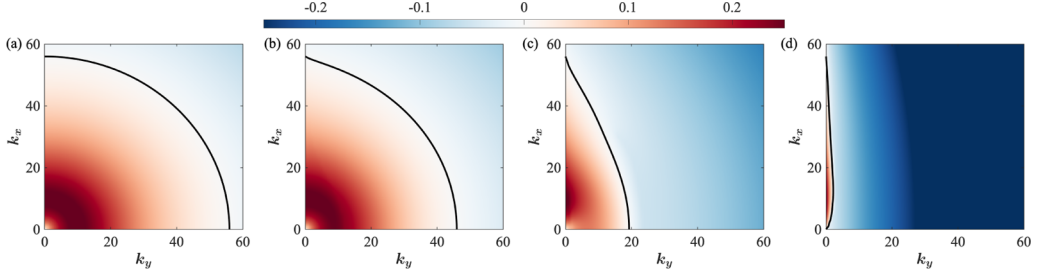
FIG. 2. The real part of the temporal growth factor ω_r in (k_y, k_x) space for three cases with $Ra = 10^7$, $\Lambda = 1$: (a) unsheared case, (b) $Ri = 10^4$, (c) $Ri = 10^2$, and (d) $Ri = 1$. The black solid line denotes the neutral line ($\omega_r = 0$).

the high-order terms, the linearized equations read

$$\partial_t u_i' + \frac{z - 1/2}{\sqrt{Ri}} \partial_y u_i' + \frac{1}{\sqrt{Ri}} \delta_{iy} u_z' = -\partial_i p' + \frac{\sqrt{Sc}}{\sqrt{Ra}} \partial_j^2 u_i' + \delta_{iz}(\Lambda \theta' - s'), \tag{4a}$$

$$\partial_t \theta' + \frac{z - 1/2}{\sqrt{Ri}} \partial_y \theta' + u_z' = \frac{\sqrt{Sc}}{\sqrt{RaPr}} \nabla^2 \theta', \tag{4b}$$

$$\partial_t s' + \frac{z - 1/2}{\sqrt{Ri}} \partial_y s' + u_z' = \frac{1}{\sqrt{RaSc}} \nabla^2 s', \tag{4c}$$

$$\partial_j u_j' = 0. \tag{4d}$$

By taking the divergence of Eq. (4a) and using the continuity condition (4d), one obtains

$$\frac{2}{\sqrt{Ri}} \partial_y u_z' = -\nabla^2 p' + \partial_z(\Lambda \theta' - s'). \tag{5}$$

To eliminate the pressure term, one can further take the z derivative of Eq. (5) and minus it by the Laplacian of the z component of Eq. (4a). A fourth-order differential equation for u_z can then be obtained as

$$\partial_t \nabla^2 u_z' = \frac{\sqrt{Sc}}{\sqrt{Ra}} \nabla^4 u_z' - \frac{z - 1/2}{\sqrt{Ri}} \partial_y \nabla^2 u_z' + \nabla_h^2(\Lambda \theta' - s'), \tag{6}$$

in which $\nabla_h^2 = \partial_x^2 + \partial_y^2$ is the Laplacian in the horizontal plane. The derivations of these linearized equations are standard and can be found in many textbooks (e.g., see Chap. 6 of [31]). Equations (4b), (4c), and (6) constitute an eigenvalue problem for three perturbation variables. We can numerically solve it by introducing a normal-mode solution as

$$\psi'(x, y, z, t) = \tilde{\psi}(z) \exp(ik_x x + ik_y y + \omega t), \tag{7}$$

in which ψ stands for u_z, θ, or s and the tilde denotes the complex vertical shape functions. k_x and k_y are the real wave numbers in the horizontal plane. $\omega = \omega_r + i\omega_i$ is the complex temporal growth factor. To solve the eigenproblem for different control parameters (Ra, Ri, Λ) and wave numbers (k_x, k_y), the Chebyshev polynomial expansion and the collocation method are adopted in the vertical direction. The resolution in the vertical direction is 300. Grid convergence has been examined by increasing the resolution to 600, and the relative difference in the growth rate is less than 0.01%.

In Fig. 2 we show the growth rates for modes with different wave numbers. The Rayleigh number is fixed at $Ra = 10^7$ and the density ratio at $\Lambda = 1.0$. Unsheared state and three different Richardson numbers are considered, i.e., $Ri = 10^4$, 10^2, and 1. The neutral curve with $\omega_r = 0$ is also plotted for each set of parameters. For the unsheared case shown in Fig. 2(a), there are very little differences

of ω_r for different directions. The most unstable mode under this condition is supposed to be the salt-finger instability. In Fig. 2(b) where the shear is very weak, the large value of ω_r concentrates a bit more on the area where $k_x > k_y$, which is due to the streamwise shear. As will be shown later, although this anisotropy is very weak, it will lead to a big change for the arrangements of the salt fingers. This phenomenon becomes clearer when Ri decreases to 10^2, as shown in Fig. 2(c). The instability along the streamwise direction is faded a lot by the shear, but it is hardly affected in the spanwise direction. When Ri equals unity in Fig. 2(d), the most unstable mode totally reduces to the area where k_y equals zero, which leads to the two-dimensional salt sheets. This result is consistent with the previous linear stability analyses [12,14]. Note that even the smallest Ri among our cases (i.e., Ri = 1) is still larger than the criterion of KH instability (Ri < 1/4), which is often considered in sheared finger studies [15,17]. Furthermore, the vertical shear profile without inflection points also indicates that the two-dimensional salt sheets are the most unstable mode [13]. Thus in the current study we do not expect a KH instability to occur and focus on the interaction only between the primary salt-finger instability and the background shear.

The streamwise shear has no effects on the pure spanwise mode ($k_y = 0$). One can easily deduce this conclusion by noticing that the terms related to Ri disappear automatically when k_y equals zero in Eqs. (4b), (4c), and (6). As the result, when the salt sheets appear, they will no longer be affected by the shear. Specifically, the width of the salt sheets is related to Ra and Λ, but independent of Ri. Thus we can choose any Ri to find the performance of ω_r with other control parameters. In this way the salt sheets behave like the two-dimensional salt fingers. For $\Lambda > 1$, by assuming $k_y = 0$ with the "tall finger" (TF) approximation [32,33] and the "viscous control" approximation [14], Eqs. (4b), (4c), and (6) can be simplified as a quadratic equation and one can just solve it and obtain

$$k_x = \left(\frac{\mathrm{RaPr}}{\mathrm{Sc}} (\Lambda - 1) \right)^{\frac{1}{4}} \tag{8}$$

for the fastest-growing modes [14]. This method applies to the unbounded domain and it is no longer available for $\Lambda \leqslant 1$ since the salt-finger instability will not happen. In our wall-bounded model, as we stated before, the salt fingers still appear when $\Lambda \leqslant 1$. Therefore we still need to use our original eigenmethod to get the most unstable modes.

Figure 3 shows ω_r as the functions of (k_x, Ra) and (k_x, Λ) with $k_y = 0$ and Ri = 10. The black dashed lines denote the most unstable modes for given Ra or Λ. In Figs. 3(a) and 3(b) the slopes of the dashed lines are about 0.13 and 0.24 for $\Lambda = 0.5$ and $\Lambda = 1$, respectively, as determined by the linear fitting. The growth rate ω_r along the line has less variation at larger Λ. In Figs. 3(c) and 3(d) the fastest-growing lines are directly compared with Eq. (8) shown by the solid lines. The coefficients obtained here are very close to the traditional method. As shown in Fig. 3(d), for fixed Ri = 10 the wave number of the most unstable mode first keeps nearly constant for $\Lambda \lesssim 0.7$ and then increases monotonically as Λ increases above unity. In Fig. 3 we also plot the wave number corresponding to the characteristic length scale extracted from the fully nonlinear DNS results (see the black dots). Specifically, we extract the width of the salt sheets, d, from flow fields and treat it as the half wavelength, i.e., corresponding to the wave number $k_x = \pi/d$. Although the exact values are different between the results of the linear analysis and the nonlinear simulations, which is totally expected, the overall trends are still quite similar.

IV. THREE-DIMENSIONAL DIRECT NUMERICAL SIMULATION

A. Numerical settings

We now turn to the fully nonlinear simulations. The numerical method will be briefly described first; then the numerical results will be discussed. We use our well-developed code to solve governing equations (2). The code employs a fraction of time step method with the finite-difference scheme. An advantage of this code is the use of the multigrid method; namely, a refined mesh is established for the salinity field because of its relatively small diffusivity, while the other variables
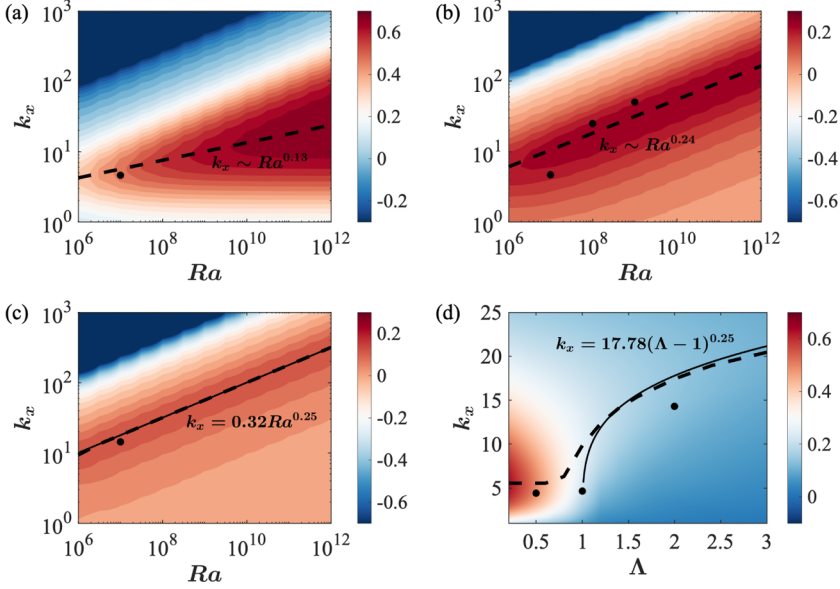
FIG. 3. The real part of the temporal growth factor ω_r as a function of (k_x, Ra) and (k_x, Λ) with (a) $\Lambda = 0.5$, (b) $\Lambda = 1$, (c) $\Lambda = 2$, and (d) $\mathrm{Ra} = 10^7$. For all panels $k_y = 0$ and $\mathrm{Ri} = 10$. The black dashed lines denote the fastest-growing modes, and dots mark the spanwise length scales of the dominant structures in DNS results, respectively. The scaling laws in (a) and (b) are given by linear fitting with slopes 0.13 and 0.24, respectively. The relationships in (c) and (d) are directly obtained from Eqs. (8) and shown by the black solid lines, respectively.

are solved on the basic mesh. The code has been widely used in our previous DDC cases and other turbulent simulations [27,34]. Initially both the temperature and salinity increase linearly from bottom to top, while velocity $\mathbf{u}$ is set to zero. Besides, small perturbations are added to trigger the flow. All the simulations have been run until the statistically steady state is reached, and the flow fields and statistical results are extracted from the statistically steady stage.

Details of the parameter setting are shown in the Appendix. Specifically, all cases are divided into five groups by the different Rayleigh number Ra and density ratio Λ. The first three groups have the same Rayleigh number $\mathrm{Ra} = 10^7$ and different density ratios $\Lambda = 0.5, 1$, and 2, respectively. Then we keep $\Lambda = 1$ and increase Ra to 10^8 and 10^9, as shown in the last two groups. Within each group, the Richardson number Ri gradually varies in a large range over five or six orders of magnitude. We would like to stress again that, although the global density ratios $\Lambda = 0.5$ and 1 do not lie in the traditional range $1 < \Lambda < \kappa_\theta/\kappa_s = 100$ where salt fingers can develop, in our wall-bounded configuration salt fingers emerge in the bulk for all the simulations since the global density ratio is not the actual density ratio of the salt-finger bulk.

B. Initial development of the salt fingers

We first investigate the development of the flow field from the beginning of the simulations. The horizontal averaged salinity $\langle s \rangle_h$ and temperature $\langle \theta \rangle_h$ profiles are displayed versus the time in Fig. 4. Three cases with different density ratios $\Lambda = 0.5, 1, 2$ at $\mathrm{Ra} = 10^7$ and $\mathrm{Ri} = 10^4$ are considered. The salinity and temperature field experienced a vertical reverse in the bulk area shortly after the simulation started, indicating a rough convection emerging. For lower Λ, this convection happens earlier and more roughly (see the variation of Reynolds number $\mathrm{Re} = |\mathbf{u}^*|H/\nu$ in the last row of Fig. 4). After the intense mixing, the temperature field quickly returns to the linear state due to its large diffusivity, while the salinity field gradually becomes homogeneous in the bulk,
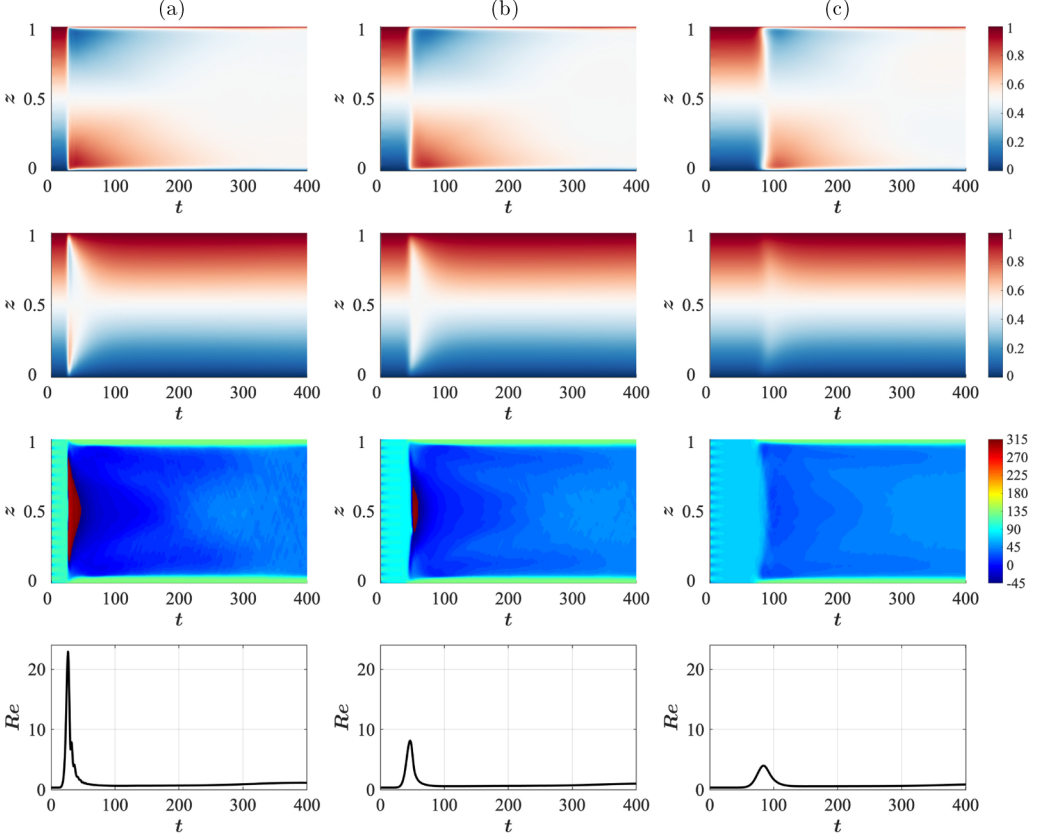
FIG. 4. The initial time evolution of the mean salinity vertical profile, the mean temperature vertical profile, the Turner angle profile, and the Reynolds number (from top to bottom), with (a) $\Lambda = 0.5$, (b) $\Lambda = 1$, and (c) $\Lambda = 2$ (from left to right). The other control parameters read $\mathrm{Ra} = 10^7$ and $\mathrm{Ri} = 10^4$.

leaving the high gradient regions near the two boundaries. To characterize the DDC flow in this period, we introduce the Turner angle defined as $\mathrm{Tu} = 135° - \arg(\beta_s \partial_z \langle s \rangle_h + i\beta_\theta \partial_z \langle \theta \rangle_h)$ [35]. In this way, the range of salt-finger instability $1 < \Lambda < 100$ becomes $45.57° < \mathrm{Tu} < 90°$. In addition, $90° < \mathrm{Tu} < 270°$ is for the gravitational unstable convection and $-45° < \mathrm{Tu} < 45°$ is for the stable stratification. In the third row of Fig. 4, we show the time evolution of Tu. The initial convection totally changes Tu, making a stable state in the bulk area and unstable convection in the boundary layers. In this situation, salt-finger instability emerges in the thin region adjacent to the boundary layers, gradually extending to the whole domain. In the follow sections we will focus on the final state of the flow field.

C. Flow morphology and transport properties at $\mathrm{Ra} = 10^7$

In this section we focus on the cases with $\mathrm{Ra} = 10^7$ and varying Λ and Ri. We first look at the morphology change of finger structures as the shear enhances for $\Lambda = 1$. Our results suggest that these qualitative behaviors are similar for different Ra and Λ. Figure 5 presents three-dimensional volume rendering of instantaneous salinity fields for five different shear rates. The left column shows the structures with salinity smaller than $0.3\Delta_s$ and larger than $0.7\Delta_s$, which include the finger structures both ascending from the bottom plate and descending from the top plate. The right column only shows the finger structures growing from the bottom plate with salinity smaller than $0.3\Delta_s$. In
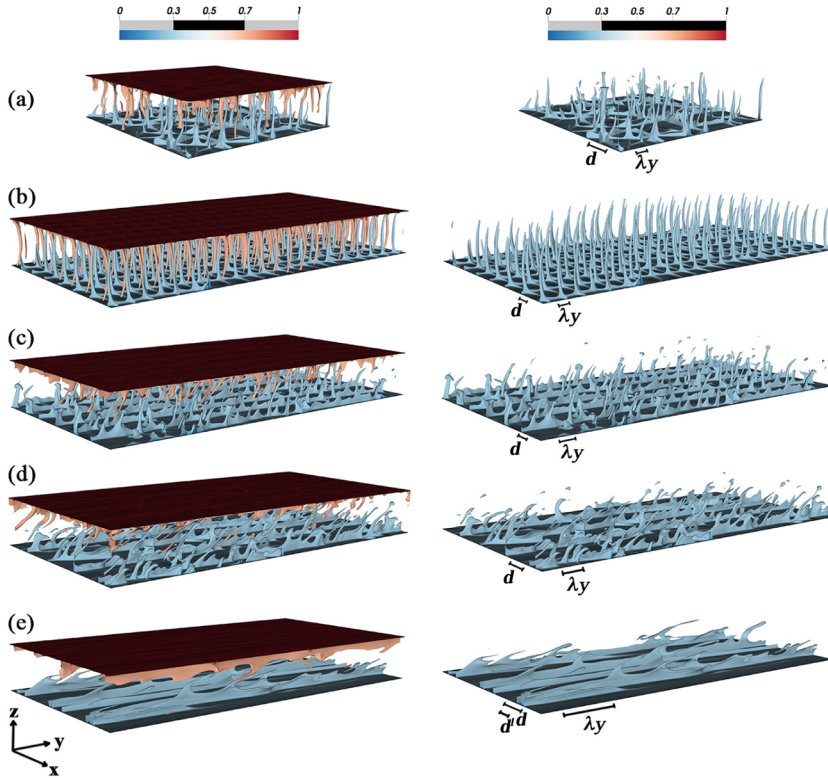
FIG. 5. Three-dimensional volume rendering of the instantaneous salinity field with (a) no background shear, (b) $Ri = 10^4$, (c) $Ri = 10^3$, (d) $Ri = 10^2$, and (e) $Ri = 10$. The color is determined by the salinity in two end values (left) and a single end value (right). The other control parameters all read $Ra = 10^7$, $\Lambda = 1$. The spanwise half wavelength d and the streamwise length scale λ_y calculated by the autocorrelation function of salinity (Fig. 6) are shown in the right column. In (e) the width d^l predicted by the linear stability analysis is also shown.

the absence of shear, as shown in Fig. 5(a), the salt fingers originating from both plates are arranged disorderly in their horizontal locations, which is similar to the previous simulations [27,36]. Due to the relatively low Ra, most of the salt fingers reach the opposite plate. Interestingly, a weak shear already has profound effects on the horizontal arrangement of the fingers. For $Ri = 10^4$, namely, when the shear velocity is only 1% of the free-fall velocity, the salt fingers are still vertically oriented but their horizontal locations become very well organized. Fingers rooted from the same plate form nearly straight lines which are along the streamwise direction. Meanwhile, ascending fingers and descending ones appear alternatively in the spanwise direction. For $Ri = 10^3$ the salt fingers exhibit distinct tilting towards the shearing direction and sheetlike structures along the streamwise direction emerge at the roots of fingers near the plates. As Ri decreases further the sheetlike structures are more clear. For $Ri = 10$, namely, the strongest shear considered here, the dominant structures become nearly two-dimensional salt sheets, as shown in Fig. 5(e). It should be noted that $Ri = 10$ is close to the typical value measured in the ocean [10]. If Ri continues to decrease, secondary instability may develop for the salt-sheet structures [18]. Above discussions indicate that as the shear strengthens first the horizontal pattern of fingers is altered, then fingers are tilted, and finally fingers are replaced by salt sheets along the streamwise direction. To quantitatively investigate such behaviors, we calculate the autocorrelation coefficient C_s of salinity in the horizontal
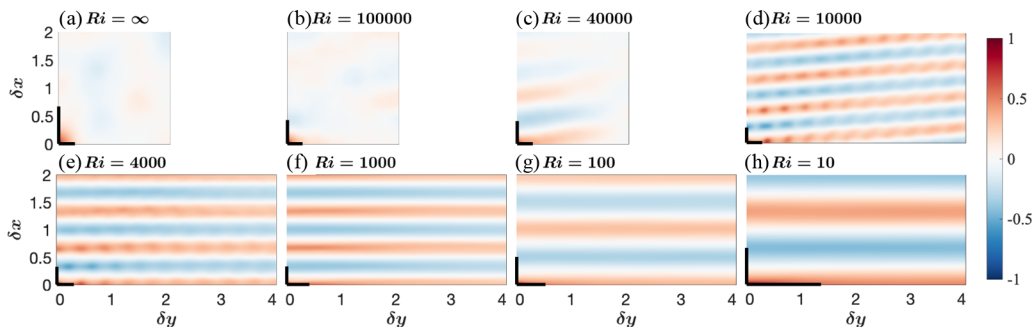
FIG. 6. The autocorrelation coefficient C_s of salinity for the streamwise separation δ_y and the spanwise separation δ_x in the vertical midplane. Different shear strengths are set as unsheared for (a) and $\mathrm{Ri} = 10^5$, 4×10^4, 10^4, 4×10^3, 10^3, 10^2, and 10 for (b–h), respectively. The other control parameters all read $\mathrm{Ra} = 10^7$, $\Lambda = 1$. The spanwise half wavelength d and the streamwise length scale λ_y are denoted by black solid lines in each panel.

directions as

$$C_s(\delta_x, \delta_y) = \frac{\langle (s(x, y) - \mu_s)(s(x + \delta_x, y + \delta_y) - \mu_s) \rangle_h}{\sigma_s^2(x, y)}, \tag{9}$$

in which μ_s and σ_s are the mean and the standard deviation of salinity over the given horizontal plane and time, respectively. Here $\langle \ \rangle_h$ stands for the temporal and spatial average over a horizontal plane. By definition $-1 \leqslant C_s \leqslant 1$ and $C_s(0, 0) = 0$. The coefficient C_s is computed for the cases with $\mathrm{Ra} = 10^7$ and $\Lambda = 1$ over the horizontal plane at the height $0.2H$. The results are shown in Fig. 6. For the case without shear, the autocorrelation coefficient is isotropic in the $(\delta x, \delta y)$ plane, as shown in Fig. 6(a). This is expected since fingers randomly distribute in the horizontal directions without any preference. When a weak shear is applied, the correlation immediately becomes stronger along the line with a small angle to the δy direction, namely, close to streamwise direction. For $\mathrm{Ri} = 10^4$ an organized pattern emerges in the contours of C_s [see Fig. 6(d)]. Patches with large positive and negative values appear with a regular spacing. Compared with Fig. 5(b), it is obvious that the organized pattern of C_s corresponds to the regularly distributed fingers. As the shear further strengthens, the organized pattern disappears and the autocorrelation coefficient is dominated by a strong strip along the δy direction, indicating streamwise-oriented sheetlike structures.

Some typical length scales can be extracted from the autocorrelation coefficient C_s. From the function $C_s(\delta x = 0, \delta y)$ one can use a parabola to fit the curve close to the original point, then a length scale λ_y can be defined as four times the intersection location of this parabola and the δy axis. Clearly λ_y is related to the decreasing rate of C_s along the δy axis and indicates the correlation length of the salinity field along the streamwise direction, as displayed straightforwardly in Figs. 5 and 6. The dependence of λ_y on the shear strength is plotted in Fig. 7. As the shear becomes stronger, namely, increasing Ri^{-1}, the streamwise correlation length first keeps constant and then increases for all three density ratios considered. This corresponds to the fact that fingers become organized at weak shear and then are replaced by sheets when shear is strong enough. Another length scale is the spanwise spacing d of the salt-finger or salt-sheet structures, which can be determined by the value of δx at the first negative minimum of the curve $C_s(\delta x, \delta y = 0)$. The results are summarized in the Appendix and also displayed in Figs. 5 and 6. When the salt sheets totally replace the finger structure, d is assumed to be the width of the sheets and independent of Ri, which is compared with the linear results in Figs. 3(b) and 5(e). It can be seen that the linear stability analysis captures the variation trend of this spanwise spacing scale. We now turn to the mean profiles of scalar fields. Figure 8 shows the vertical profiles of salinity and temperature averaged both in time and over the horizontal plane. Three cases are shown for $(\mathrm{Ra}, \Lambda) = (10^7, 1)$ and $\mathrm{Ri} = \infty$, 1000, and
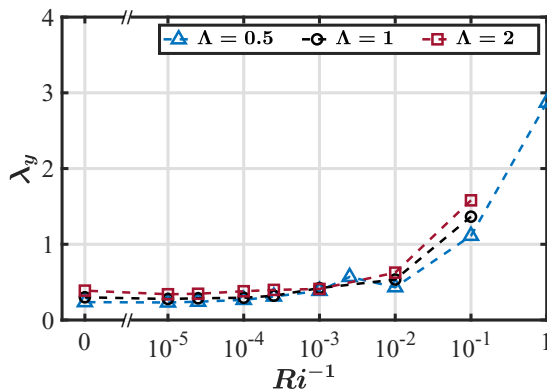
FIG. 7. The streamwise correlation length scale determined from the autocorrelation function versus the shear strength. For all cases Ra is fixed at 10^7.

10, respectively. The salinity field has distinct boundary layers and bulk regions [see Fig. 8(a)]. Due to the large thermal diffusivity, the temperature profiles are very close to the linear one, as shown in Fig. 8(b). As the shear becomes stronger, the vertical gradient of mean salinity around the mid-height changes from slightly positive to negative, and then becomes positive again. We calculate the salinity vertical gradient averaged in the middle bulk area for each case, i.e., $\langle \partial_z \bar{s} \rangle_b = (\langle \bar{s} \rangle_{z=0.6} - \langle \bar{s} \rangle_{z=0.4})/0.2$. The results are summarized in the Appendix and plotted in Fig. 9(a). The profiles for the standard deviation of salinity and temperature are shown in Figs. 8(c) and 8(d). For the weak shear case with negative mean salinity gradient at the center, the fluctuations of both scalars are also weaker compared to other cases. Moreover, the salinity boundary layer thickness λ_s can be calculated by the maximum value points in Fig. 8(c), and its variations are shown in Fig. 9(b).

The nonmonotonic variations of both $\langle \partial_z \bar{s} \rangle_b$ and λ_s can be understood by the changing of the flow morphology and the salinity field near the boundary. In Fig. 10 we plot the salinity contour on the horizontal plane $z/H = 0.9$, which is close to the upper boundary. With a weak shear salt fingers become very well organized in their horizontal locations, and more fingers with relatively low salinity can rise to the height very close to the top boundary, which can be seen by comparing
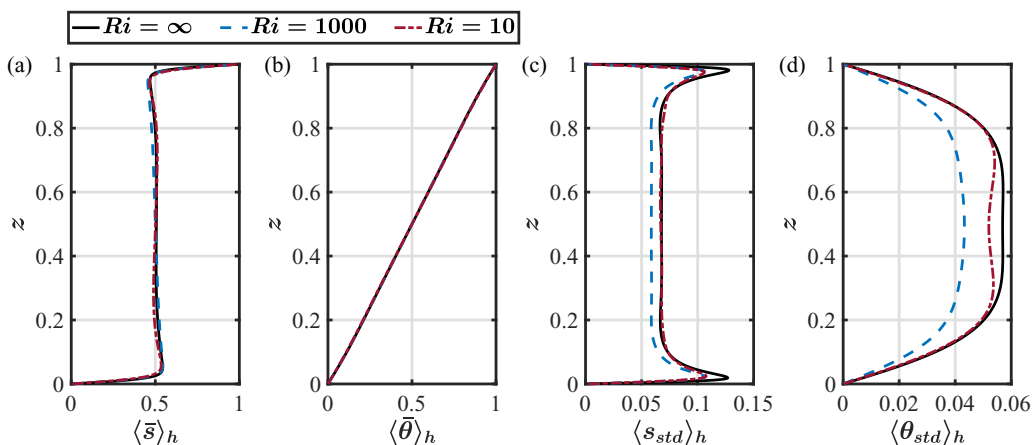

FIG. 8. The mean profiles of (a) salinity, (b) temperature, (c) standard deviation of salinity, and (d) standard deviation of temperature. The bar and the bracket stand for the temporal and horizontal average value, respectively. In each panel three cases with Ra = 10^7, $\Lambda = 1$ and different shear strengths are shown.
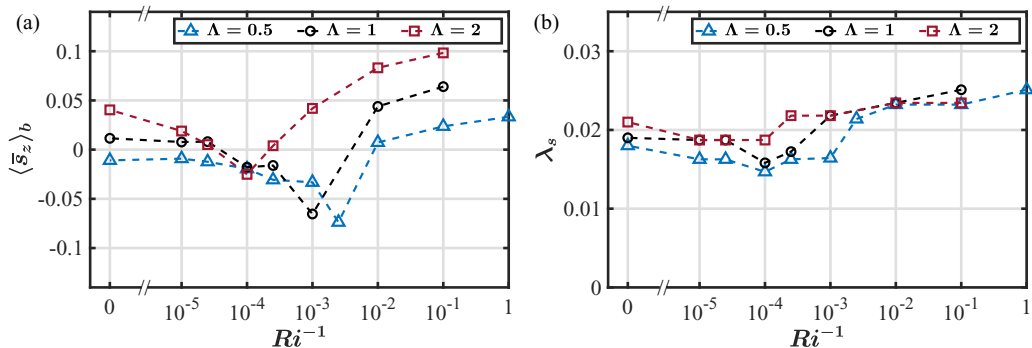
FIG. 9. (a) The central salinity gradient $\langle \partial_z \bar{s} \rangle_b$ vs Ri^{-1}. (b) The salinity boundary layer thickness λ_s vs Ri^{-1}. For all cases Ra is fixed at 10^7.

Figs. 10(a) and 9(b). These rising fingers stop growing as they reach the upper boundary layer, at which height they reduce the mean salinity and enhance the fluctuation or standard deviation of the salinity field. Similar behaviors occur for the descending fingers with high salinity as they reach the lower boundary layer. These effects cause the negative gradient in the bulk and shift the peak locations in the standard deviation profiles towards the corresponding boundary. With the strong shear, as in the case shown in Fig. 10(c), the salt fingers cannot reach the opposite boundary, resulting in the positive mean gradient in salinity and thicker boundary layer.

The change of structure morphology affects the vertical transport property of the system. Three nondimensional numbers are used to measure the heat, salt, and momentum fluxes, namely, the two Nusselt numbers and the vertical Reynolds number defined as

$$\mathrm{Nu}_\theta = \left| \frac{\langle u_z \theta \rangle_h - \kappa_\theta \partial_z \langle \theta \rangle_h}{\kappa_\theta \Delta_\theta H^{-1}} \right|, \quad \mathrm{Nu}_s = \left| \frac{\langle u_z s \rangle_h - \kappa_s \partial_z \langle s \rangle_h}{\kappa_s \Delta_s H^{-1}} \right|, \quad \mathrm{Re}_z = \frac{u_z^{rms} H}{\nu}. \tag{10}$$

Note that we calculate the Reynolds number by the root-mean-square value of the vertical velocity u_z to measure the vertical momentum transport. These quantities are plotted in Fig. 11. Interestingly, both Nu_s and Re_z first increase and then decrease as Ri^{-1} gradually increases. That is, for weak shear, both salinity transfer and vertical motion are enhanced, while they are suppressed for stronger shear. The enhancement of these two quantities is caused by the organized fingers which generate a more efficient transport than the no-shear case. Similar phenomena have also been reported in other systems [37]. The heat Nusselt number, however, only exhibits a very weak variation for different
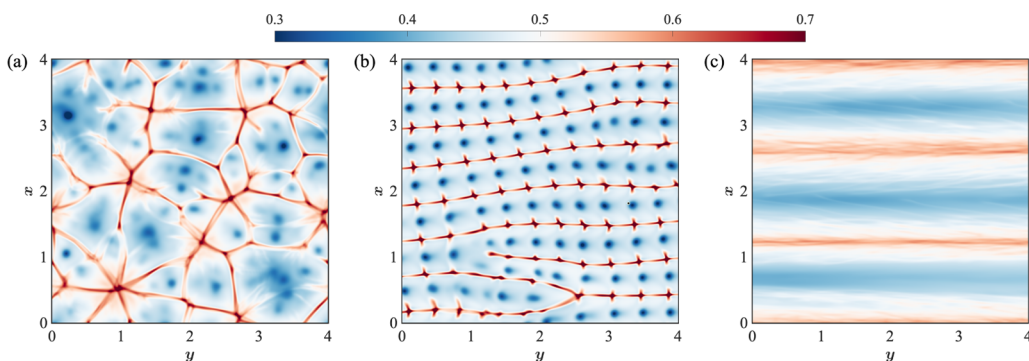

FIG. 10. The time-averaged salinity contour in the $z = 0.9$ plane for (a) the unsheared case, (b) $\mathrm{Ri} = 10^4$, and (c) $\mathrm{Ri} = 10$. For all the cases $\mathrm{Ra} = 10^7$, $\Lambda = 1$.
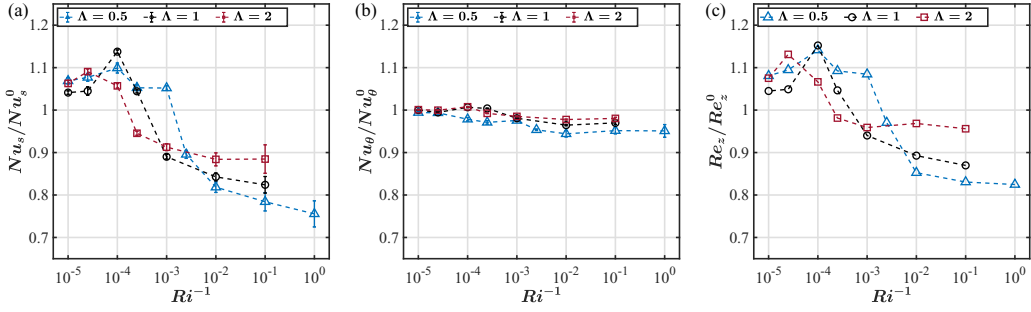
FIG. 11. The global fluxes for different shear strengths normalized by the values of no-shear cases. (a) Salinity Nusselt number, (b) heat Nusselt number, and (c) Reynolds number. For all cases Ra is fixed at 10^7. For $\Lambda = (0.5, 1, 2)$, $Nu_s^0 = (33.8, 32.3, 31.0)$, $Nu_\theta^0 = (1.32, 1.17, 1.09)$, and $Re_z^0 = (0.93, 0.78, 0.65)$.

shear strengths. This is expectable since in the current setting heat diffuses much quicker than salt. For the relatively low Ra = 10^7, diffusion dominates the heat transport and shear only has a minor influence.

D. Influences of different Rayleigh numbers

We now investigate the influences of the Rayleigh number. Λ is fixed at unity and three Rayleigh numbers are considered, namely, Ra = 10^7, 10^8, and 10^9. As discussed in the previous section, for all the Ra and Λ considered here, the flow morphology shows a similar transition as those shown in Fig. 5. Here, Fig. 12 presents the three-dimensional volume rendering of the instantaneous salinity field with Ra = 10^8 and 10^9 for Ri = 10^4. It should be pointed out that the salt fingers have similar strength between those ascending from the bottom and those descending from the top. The regularity of the flow structures weakens with the increase of Ra for the same shear strength. Moreover, the salt fingers become more turbulent and quickly lose their salinity anomaly before reaching the opposite boundary. In Fig. 13 we plot the behaviors of λ_y versus Ri^{-1} for the three different Ra. For all Rayleigh numbers the streamwise correlation length increases as shear becomes stronger, indicating the formation of sheetlike structures. However, λ_y is smaller for larger Ra. Moreover, even for the strongest shear with Ri = 10 the increment of λ_y with respect to the no-shear case is rather small; i.e., the coherence of the salt-sheet structures is still quite weak. For higher Rayleigh number as in the ocean, the salt-sheet structures may only develop at even stronger shear.

Different behaviors of the correlation length scales also reflect themselves in the variations of fluxes. In Fig. 14 we plot the two Nusselt numbers and the Reynolds number, all normalized by the
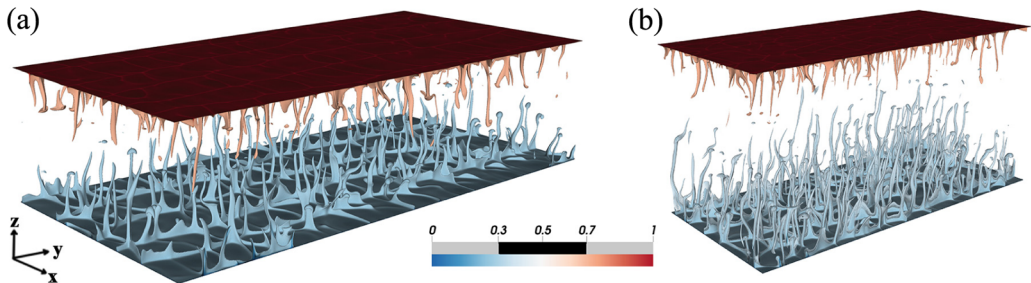

FIG. 12. Three-dimensional volume rendering of the instantaneous salinity field with (a) Ra = 10^8 and (b) Ra = 10^9. The other control parameters read Ri = 10^4, $\Lambda = 1$.
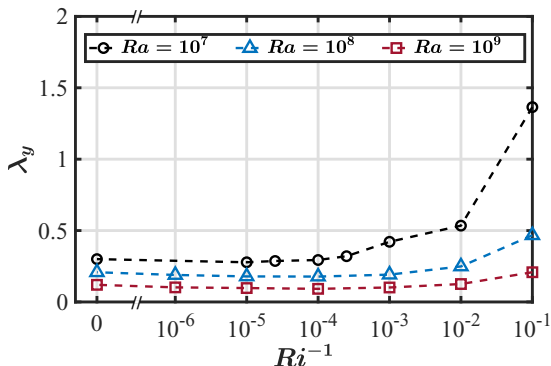
FIG. 13. The streamwise correlation length scale determined from the autocorrelation function versus the shear strength. Λ is fixed at 1.

values of the no-shear cases. For Ra $= 10^7$, both Nu$_s$ and Re$_z$ are enhanced considerably for weak shear. However, this enhancement is smaller as Ra becomes larger. For Ra $= 10^9$ there is effectively no enhancement in Nu$_s$. This can be attributed to less coherence of salt-finger structures along the vertical direction at high Ra. At the strongest shear studied here, Nu$_s$ can be almost 20% less than that of the no-shear case. The reduction in heat flux is larger for higher Ra and stronger shear. With strong buoyancy driving force, convection starts to play an apparent role in the dynamics of temperature component, instead of the nearly conduction state for Ra $= 10^7$. And then shear can affect the heat flux.

V. CONCLUSIONS

In summary, the salt-finger DDC with a uniform shear is studied by both linear stability analysis and fully nonlinear simulation. We demonstrate that a weak shear can already alter the flow morphology significantly. Specifically, salt fingers distribute regularly when a weak shear is applied. As the background shear further increases, the dominant structures change to salt sheets parallel to the shearing velocity, and the structures become increasingly correlated along the streamwise direction. For the current flow bounded by two plates from top and bottom, linear stability analyses reveal a similar trend: the most unstable modes become two dimensional as shear is enhanced. For $\Lambda > 1$, the spanwise scales of the most unstable modes predicted by the linear theory for the current
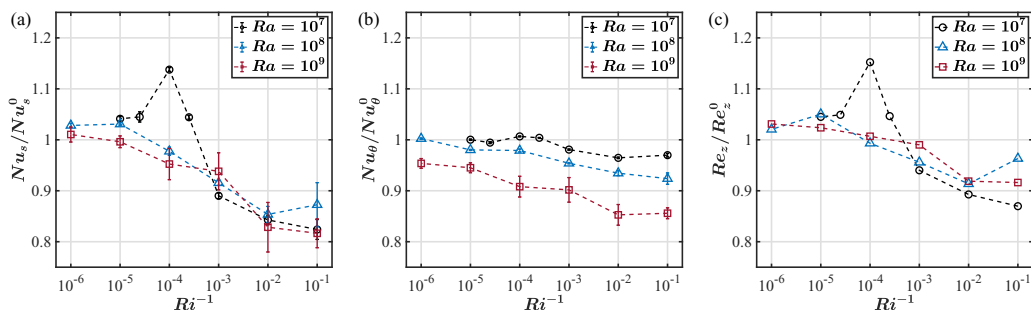

FIG. 14. The global fluxes for different shear strengths normalized by the values of no-shear cases. (a) Salinity Nusselt number, (b) heat Nusselt number, and (c) Reynolds number. Λ is fixed at 1. For Ra $= (10^7, 10^8, 10^9)$, Nu$_s^0 = (32.3, 63.8, 135)$, Nu$_\theta^0 = (1.17, 1.35, 1.77)$, Re$_z^0 = (0.78, 2.02, 5.50)$.

wall-bounded model show similar behaviors as those found in previous sheared salt-finger studies, i.e., $k_x \sim \mathrm{Ra}^{0.25}(\Lambda - 1)^{0.25}$. For $\Lambda = 1$ and $\Lambda = 0.5$, the exponent of Ra decreases to 0.24 and 0.13, respectively. For all the parameters considered here, their overall variations are also consistent with those obtained from the current nonlinear simulations of fully developed flows.

The effects of shear on global transports are rather complex. The salinity Nusselt number first increases when a weak shear is applied. The enhancement of Nu_S is related to the regularization of salt-finger distribution under weak shear. In this regime, fingers carry more salinity from one plate to another, which produces the salinity reverse near the boundary layer. The magnitude of this enhancement reduces for larger Ra. When the shear is strong enough, salinity flux is suppressed. Nu_S decreases by about 20% for the strongest shear considered here. At low Ra the thermal field is effectively in the conductive state, and the temperature Nusselt number only decreases slightly as shear becomes stronger. For the highest Ra considered here, the decrement of Nu_θ becomes notable for strong shear.

Our results not only reveal interesting results about the fingering DDC with weak shear, but also have important implications for oceanic DDC. In particular, even a weak shear can notably alter the heat and salt fluxes in the vertical direction. Moreover, it affects the two fluxes in different ways; therefore, also the density flux ratio is changed.

ACKNOWLEDGMENTS

APPENDIX: NUMERICAL DETAILS

In this Appendix we provide the summary of the control parameters, key numerical details, and the responses for all simulation cases. Each group of cases is listed in each of Tables I–V for a combination of Rayleigh number Ra and density ratio Λ as indicated in the caption. For all simulations, we keep the length in the vertical direction $L_z = 1$, the Prandtl number $\mathrm{Pr} = 7$, and the Schmidt number $\mathrm{Sc} = 700$, respectively.

TABLE I. Cases for Ra $= 10^7$ and $\Lambda = 0.5$. Columns from left to right are the Richardson number, domain sizes in the spanwise and streamwise directions, resolutions in the spanwise, streamwise, and normal directions (with refinement factors for multiple resolutions), the streamwise correlation length scale, the spanwise spacing scale, the bulk-averaged vertical gradient of salinity, the salinity boundary layer thickness, the salinity and temperature Nusselt numbers, and the vertical Reynolds number, respectively.

Ri	L_x	L_y	$N_x(m_x)$	$N_y(m_y)$	$N_z(m_z)$	λ_y	d	$\langle \partial_z \bar{s} \rangle_b$	λ_s	Nu_s	Nu_θ	Re_z
1×10^0	4	8	192(4)	384(5)	128(2)	2.872	0.711	0.033	0.025	25.6	1.26	0.77
1×10^1	4	8	192(4)	384(5)	128(2)	1.112	0.680	0.024	0.023	26.5	1.26	0.77
1×10^2	4	8	192(4)	384(5)	128(2)	0.432	0.680	0.007	0.023	27.7	1.25	0.79
4×10^2	4	8	192(4)	384(5)	128(2)	0.568	0.346	-0.074	0.021	30.3	1.26	0.90
1×10^3	4	4	256(4)	256(4)	128(3)	0.384	0.354	-0.033	0.016	35.6	1.29	1.01
4×10^3	4	4	256(4)	256(4)	128(2)	0.312	0.318	-0.031	0.016	35.6	1.26	1.02
1×10^4	4	4	256(4)	256(4)	128(2)	0.268	0.299	-0.020	0.015	37.2	1.30	1.06
4×10^4	4	4	256(4)	256(4)	128(2)	0.240	0.381	-0.012	0.016	36.4	1.32	1.02
1×10^5	4	4	192(4)	192(4)	128(2)	0.232	0.445	0.009	0.016	36.2	1.32	1.01
∞	4	4	192(4)	192(4)	128(2)	0.236	0.904	-0.011	0.018	33.8	1.32	0.93

TABLE II. Cases for Ra $= 10^7$ and $\Lambda = 1$. Columns are the same as those in Table I.

Ri	L_x	L_y	$N_x(m_x)$	$N_y(m_y)$	$N_z(m_z)$	λ_y	d	$\langle\partial_z\bar{s}\rangle_b$	λ_s	Nu$_s$	Nu$_\theta$	Re$_z$
1×10^1	4	8	288(3)	288(4)	144(2)	1.365	0.674	0.064	0.025	26.7	1.14	0.67
1×10^2	4	8	288(3)	288(4)	144(2)	0.535	0.512	0.044	0.023	27.3	1.13	0.69
1×10^3	4	8	288(3)	288(4)	144(2)	0.421	0.336	-0.065	0.022	28.8	1.15	0.73
4×10^3	4	8	288(3)	288(4)	144(2)	0.321	0.331	-0.016	0.017	33.8	1.18	0.81
1×10^4	4	8	288(3)	288(4)	144(2)	0.294	0.285	-0.018	0.016	36.8	1.18	0.89
4×10^4	4	4	288(3)	288(3)	144(2)	0.287	0.414	0.008	0.019	33.8	1.17	0.81
1×10^5	4	4	288(3)	288(3)	144(2)	0.278	0.433	0.008	0.019	33.7	1.17	0.81
∞	4	4	288(3)	288(3)	144(2)	0.300	0.674	0.012	0.019	32.3	1.17	0.78

TABLE III. Cases for Ra $= 10^7$ and $\Lambda = 2$. Columns are the same as those in Table I.

Ri	L_x	L_y	$N_x(m_x)$	$N_y(m_y)$	$N_z(m_z)$	λ_y	d	$\langle\partial_z\bar{s}\rangle_b$	λ_s	Nu$_s$	Nu$_\theta$	Re$_z$
1×10^1	4	8	288(3)	288(4)	144(2)	1.580	0.220	0.098	0.023	27.4	1.07	0.62
1×10^2	4	8	288(3)	288(4)	144(2)	0.624	0.215	0.083	0.023	27.4	1.07	0.63
1×10^3	4	8	288(3)	288(4)	144(2)	0.412	0.326	0.042	0.022	28.3	1.07	0.62
4×10^3	4	8	288(3)	288(4)	144(2)	0.400	0.280	0.004	0.022	29.3	1.08	0.64
1×10^4	4	8	288(3)	288(4)	144(2)	0.380	0.252	-0.025	0.019	32.8	1.10	0.69
4×10^4	4	4	288(3)	288(3)	144(2)	0.348	0.220	0.005	0.019	33.8	1.09	0.74
1×10^5	4	4	288(3)	288(3)	144(2)	0.340	0.303	0.019	0.019	32.9	1.09	0.70
∞	4	4	288(3)	288(3)	128(2)	0.388	1.243	0.040	0.021	31.0	1.09	0.65

TABLE IV. Cases for Ra $= 10^8$ and $\Lambda = 1$. Columns are the same as those in Table I.

Ri	L_x	L_y	$N_x(m_x)$	$N_y(m_y)$	$N_z(m_z)$	λ_y	d	$\langle\partial_z\bar{s}\rangle_b$	λ_s	Nu$_s$	Nu$_\theta$	Re$_z$
1×10^1	4	8	384(3)	768(3)	192(2)	0.468	0.127	0.075	0.011	55.6	1.25	1.95
1×10^2	4	8	384(3)	768(3)	192(2)	0.248	0.373	0.051	0.011	54.4	1.26	1.85
1×10^3	4	8	384(3)	768(3)	192(2)	0.192	0.352	0.012	0.011	58.4	1.29	1.93
1×10^4	4	8	384(3)	768(3)	192(2)	0.176	0.217	-0.001	0.010	62.3	1.33	2.01
1×10^5	4	4	480(3)	480(3)	192(2)	0.180	0.357	0.002	0.009	65.7	1.33	2.12
1×10^6	4	4	384(3)	384(3)	192(2)	0.188	0.401	0.001	0.009	65.5	1.36	2.06
∞	4	4	384(3)	384(3)	192(2)	0.208	0.589	0.001	0.009	63.8	1.35	2.02

TABLE V. Cases for Ra $= 10^9$ and $\Lambda = 1$. Columns are the same as those in Table I.

Ri	L_x	L_y	$N_x(m_x)$	$N_y(m_y)$	$N_z(m_z)$	λ_y	d	$\langle\partial_z\bar{s}\rangle_b$	λ_s	Nu$_s$	Nu$_\theta$	Re$_z$
1×10^1	1	2	240(4)	480(4)	288(3)	0.208	0.062	0.121	0.005	110	1.51	5.04
1×10^2	1	2	240(4)	480(4)	288(3)	0.124	0.061	0.059	0.005	112	1.51	5.05
1×10^3	1	2	240(4)	480(4)	288(3)	0.100	0.069	0.038	0.005	126	1.59	5.45
1×10^4	1	2	240(4)	480(4)	288(3)	0.092	0.068	0.019	0.005	128	1.60	5.54
1×10^5	1	2	240(4)	480(4)	288(3)	0.096	0.077	0.009	0.004	134	1.67	5.63
1×10^6	1	1	240(4)	240(4)	288(3)	0.104	0.084	0.012	0.004	136	1.69	5.67
∞	1	1	240(4)	240(4)	288(3)	0.120	0.331	0.005	0.005	135	1.77	5.50

[1] J. S. Turner, Double-diffusive phenomena, Annu. Rev. Fluid Mech. **6**, 37 (1974).

[2] R. W. Schmitt, Double diffusion in oceanography, Annu. Rev. Fluid Mech. **26**, 255 (1994).

[3] Y. You, A global ocean climatological atlas of the Turner angle: Implications for double-diffusion and water-mass structure, Deep Sea Res., Part I **49**, 2075 (2002).

[4] R. W. Schmitt, J. R. Ledwell, E. T. Montgomery, K. L. Polzin, and J. M. Toole, Enhanced diapycnal mixing by salt fingers in the thermocline of the tropical atlantic, Science **308**, 685 (2005).

[5] M. E. Stern, The "salt-fountain" and thermohaline convection, Tellus **12**, 172 (1960).

[6] T. Radko, *Double-Diffusive Convection* (Cambridge University Press, Cambridge, UK, 2013).

[7] P. Garaud, Double-diffusive convection at low Prandtl number, Annu. Rev. Fluid Mech. **50**, 275 (2018).

[8] E. Kunze, A. J. Williams III, and R. W. Schmitt, Optical microstructure in the thermohaline staircase east of barbados, Deep-Sea Res., Part A **34**, 1697 (1987).

[9] E. Kunze, The evolution of salt fingers in inertial wave shear, J. Mar. Res. **48**, 471 (1990).

[10] M. C. Gregg and T. B. Sanford, Shear and turbulence in thermohaline staircases, Deep-Sea Res., Part A **34**, 1689 (1987).

[11] L. St. Laurent and R. Schmitt, The contribution of salt fingers to vertical mixing in the North Atlantic tracer release experiment, J. Phys. Oceanogr. **29**, 1404 (1999).

[12] P. F. Linden, Salt fingers in a steady shear flow, Geophys. Fluid Dyn. **6**, 1 (1974).

[13] S. Thangam, A. Zebib, and C. Chen, Salt-finger convection in shear flow, Phys. Fluids **27**, 804 (1984).

[14] W. D. Smyth and S. Kimura, Instability and diapycnal momentum transport in a double-diffusive, stratified shear layer, J. Phys. Oceanogr. **37**, 1551 (2007).

[15] T. Radko and M. Stern, Finescale instabilities of the double-diffusive shear flow, J. Phys. Oceanogr. **41**, 571 (2011).

[16] S. Kimura and W. Smyth, Direct numerical simulation of salt sheets and turbulence in a double-diffusive shear layer, Geophys. Res. Lett. **34**, L21610 (2007).

[17] W. D. Smyth and S. Kimura, Mixing in a moderately sheared salt-fingering layer, J. Phys. Oceanogr. **41**, 1364 (2011).

[18] W. D. Smyth and S. Kimura, Secondary instability of salt sheets, J. Mar. Res. **69**, 57 (2011).

[19] T. Radko, J. Ball, J. Colosi, and J. Flanagan, Double-diffusive convection in a stochastic shear, J. Phys. Oceanogr. **45**, 3155 (2015).

[20] A. M. Fernandes and R. Krishnamurti, Salt finger fluxes in a laminar shear flow, J. Fluid Mech. **658**, 148 (2010).

[21] S. Kimura, W. Smyth, and E. Kunze, Turbulence in a sheared, salt-fingering-favorable environment: Anisotropy and effective diffusivities, J. Phys. Oceanogr. **41**, 1144 (2011).

[22] P. H. Sichani, C. Marchioli, F. Zonta, and A. Soldati, Shear effects on scalar transport in double diffusive convection, J. Fluids Eng. **142**, 121105 (2020).

[23] M. G. Wells, R. W. Griffiths, and J. S. Turner, Generation of density fine structure by salt fingers in a spatially periodic shear, J. Geophys. Res. **106**, 7027 (2001).

[24] A. Blass, X. Zhu, R. Verzicco, D. Lohse, and R. J. Stevens, Flow organization and heat transfer in turbulent wall sheared thermal convection, J. Fluid Mech. **897**, A22 (2020).

[25] A. Blass, P. Tabak, R. Verzicco, R. J. Stevens, and D. Lohse, The effect of Prandtl number on turbulent sheared thermal convection, J. Fluid Mech. **910**, A37 (2021).

[26] T.-C. Jin, J.-Z. Wu, Y.-Z. Zhang, Y.-L. Liu, and Q. Zhou, Shear-induced modulation on thermal convection over rough plates, J. Fluid Mech. **936**, A28 (2022).

[27] Y. Yang, R. Verzicco, and D. Lohse, Scaling laws and flow structures of double diffusive convection in the finger regime, J. Fluid Mech. **802**, 667 (2016).

[28] E. Hage and A. Tilgner, High Rayleigh number convection with double diffusive fingers, Phys. Fluids **22**, 076603 (2010).

[29] M. Kellner and A. Tilgner, Transition to finger convection in double-diffusive convection, Phys. Fluids **26**, 094103 (2014).

[30] Y. Yang, R. Verzicco, and D. Lohse, From convection rolls to finger convection in double-diffusive turbulence, Proc. Natl. Acad. Sci. USA **113**, 69 (2016).

[31] P. G. Drazin, *Introduction to Hydrodynamic Stability* (Cambridge University Press, Cambridge, UK, 2002), Vol. 32.

[32] M. E. Stern, *Ocean Circulation Physics* (Academic Press, New York, 1975).

[33] R. W. Schmitt, Triangular and asymmetric salt fingers, J. Phys. Oceanogr. **24**, 855 (1994).

[34] R. Ostilla Mónico, E. P. van der Poel, R. Verzicco, S. Grossmann, and D. Lohse, Exploring the phase diagram of fully turbulent Taylor-Couette flow, J. Fluid Mech. **761**, 1 (2014).

[35] B. Ruddick, A practical indicator of the stability of the water column to double-diffusive activity, Deep-Sea Res., Part A **30**, 1105 (1983).

[36] Y. Yang, E. P. van der Poel, R. Ostilla-Mónico, C. Sun, R. Verzicco, S. Grossmann, and D. Lohse, Salinity transfer in bounded double diffusive convection, J. Fluid Mech. **768**, 476 (2015).

[37] K. L. Chong, Y. Yang, S.-D. Huang, J.-Q. Zhong, R. J. A. M. Stevens, R. Verzicco, D. Lohse, and K.-Q. Xia, Confined Rayleigh-Bénard, Rotating Rayleigh-Bénard, and Double Diffusive Convection: A Unifying View on Turbulent Transport Enhancement through Coherent Structure Manipulation, Phys. Rev. Lett. **119**, 064501 (2017).